



HAL
open science

Sea-level stability over geological time owing to limited deep subduction of hydrated mantle

N. G. Cerpa, D. Arcay, J. A. Padrón-Navarta

► **To cite this version:**

N. G. Cerpa, D. Arcay, J. A. Padrón-Navarta. Sea-level stability over geological time owing to limited deep subduction of hydrated mantle. *Nature Geoscience*, 2022, 15, pp.423-428. 10.1038/s41561-022-00924-3 . insu-03690270

HAL Id: insu-03690270

<https://insu.hal.science/insu-03690270>

Submitted on 24 Nov 2022

HAL is a multi-disciplinary open access archive for the deposit and dissemination of scientific research documents, whether they are published or not. The documents may come from teaching and research institutions in France or abroad, or from public or private research centers.

L'archive ouverte pluridisciplinaire **HAL**, est destinée au dépôt et à la diffusion de documents scientifiques de niveau recherche, publiés ou non, émanant des établissements d'enseignement et de recherche français ou étrangers, des laboratoires publics ou privés.

Sea-level stability over geological time owing to limited deep subduction of hydrated mantle

Cerpa N. G.^{1,2,*}, Arcay, D.¹, Padrón-Navarta, J. A.^{1,3}

¹Géosciences Montpellier, University of Montpellier, CNRS, University of Antilles, 34095 Montpellier Cedex 05, France

²Geoazur, Université Côte d'Azur, CNRS, Observatoire de la Côte d'Azur, IRD, 250 Avenue Albert Einstein, 06560 Valbonne, France.

³Instituto Andaluz de Ciencias de la Tierra, CSIC – University of Granada, Armilla, Granada, Spain

* : corresponding author (e-mail : nestor.cerpa@umontpellier.fr)

Liquid surface oceans are a seemingly unique feature of Earth. Long-term, global sea level depends on the balance of water fluxes between Earth's mantle and surface: between mantle degassing through volcanism and mantle regassing via the subduction of hydrous minerals. However, the overall balance of these fluxes at geological timescales remains uncertain. Geological observations suggest the stability of the long-term sea level and thus a near-steady-state regassing–degassing balance. In contrast, according to current thermopetrological modelling, the global input of H₂O inferred from geophysical observations leads to an unequivocal excess of regassing relative to degassing. Here we use recent experimental high-pressure data on natural hydrated peridotites to update the thermopetrological models and to reassess the calculations of H₂O fluxes into the mantle via subduction. Our models of 56 subduction transects show that a global input of $15\text{--}20 \times 10^8$ Tg H₂O every million years yields a limited global mantle regassing of $2.0\text{--}3.5 \times 10^8$ Tg H₂O every million years. The regassing occurs exclusively via the hydrated lithospheric mantle of the coldest subducting plates. Our requantification of the H₂O budget associated with subduction matches the estimations of mantle degassing and suggests that global sea levels have been relatively stable over geological timescales.

The water exchange between the Earth's surface and the deep interior is crucial for the evolution of our planet. Hydrous components affect mantle rheology¹ and allow Earth-like plate tectonics², while liquid-surface water is essential for planet habitability³. The mantle degasses H₂O through volcanism. Mantle regassing occurs via the subduction of H₂O chemically bound to hydrous minerals. However, metamorphic reactions with increasing temperature (T) and pressure (P) partly liberate this H₂O from the subducting oceanic plates. The fraction of the H₂O that is retained in the slab returns to the deep mantle but its proportion remains debated. At first order, the imbalance between mantle degassing and regassing exerts a first-order control on the long-term eustatic sea-level⁴. Hence, a precise quantification of the subducted H₂O fluxes is required to decipher the global water cycle.

The most comprehensive study on H₂O fluxes at present-day subduction zones⁵ estimated a Global H₂O/Water Retention (GWR) of 3.4×10^8 Tg/Myr beyond a 230-km depth. Their thermopetrological models predicted that half of the retention was controlled by the mafic crust, and a third by the hydrated lithospheric mantle, assumed to be only 2 km thick worldwide at subduction zone trenches. Because mantle degassing is approximately 2×10^8 Tg/Myr^{6,7}, the predicted GWR would have decreased the global mean sea level by approximately 100 m over the Phanerozoic⁶ (last 540 Ma, if constant over time). This is, however, close to the upper bound of retention ensuring a modest sea-level decrease (<100 m) during this Eon, as inferred from stratigraphic constraints^{6,8,9,10} (Extended Data Fig. 1).

Furthermore, reconstructions of time-dependent subduction rates in the Phanerozoic suggest that GWR was higher during specific events, e.g., during the rift pulse at approximately 150 Ma¹⁰. A GWR at present-day of 3.4×10^8 Tg/Myr or higher, as predicted by current thermopetrological models^{5,12,13,14}, seems thus inconsistent with a time-integrated low imbalance between mantle degassing and regassing. Only studies neglecting H₂O transfer via the hydrated mantle were able to reach such a criterion¹⁵. The growing evidence of an hydrated lithospheric mantle thicker than 2 km^{16,17,18,19} (see also Supplementary Information S3), as well as the potential ability of metasomatized ultramafic rocks at the slab-mantle interface to convey H₂O to the mid-mantle²⁰, urge the need to address this paradox.

The mineralogical changes in the subducting mafic crust and ultramafic mantle, control the deep-H₂O fluxes. Hence, quantitative studies of GWR rely on state-of-the-art petrological modeling of subducted hydrated lithologies.

Lawsonite is the main H₂O carrier in the crust beyond subarc depths (Fig. 1a). Its stability field is relatively well known from experimental studies^{21,22}. In contrast, the postarc main hydrous phases for ultramafic systems are far less constrained^{23,24}. The large uncertainties partly arise from the difficulty in handling laboratory H₂O-rich experiments with natural samples at mid-upper mantle depth conditions. This is evidenced by the lack of experimental data on hydrous peridotite in the 6-8 GPa range (Supp. Info. Fig. S2b). Moreover, the poorly constrained effect of some minor elements (such as Al) and the unknown prevailing oxidation state of ultramafic rocks under high-PT conditions^{24,25} preclude a proper petrological thermodynamic modeling of subducted ultramafic rocks. Consequently, experimental and modeled phase diagrams differ at pressures above 6 GPa (Fig. 1b,c and Fig. S2a,b).

Here, we improve the estimation of present-day GWR using recent experimental results on the stability of hydrous phases in natural hydrated peridotites. By considering the new experimental findings in naturally complex systems at high PT conditions²⁴, the current view of relatively large amounts of H₂O reinjected into the deep upper mantle is challenged.

Thermopetrological modeling of present-day subduction zones

We model the thermal state of all present-day subduction zones (56 subduction transects²⁶, see Methods). We use the thermodynamic database ref. 27 and code `Perple_X`²⁸ to build phase diagrams, assuming bulk compositions relevant for the crustal and mantle layers at the subduction trenches (“basalt”, Fig S5a, “gabbro” and “simplified peridotite model” Fig. 1a,b). To enhance the accuracy of the modeled mineralogical evolution of hydrated peridotites up to mid-mantle depths, we combine thermodynamic modeling to experimentally-derived assemblages from naturally complex systems²⁴ and we build a hybrid-phase diagram (“complex peridotite model” Fig. 1c, see Methods).

At shallow depths, H₂O subduction in the crustal layers occurs via amphibole, and at subarc to postarc depths via lawsonite³⁰. At the depth where the slab surface starts dragging the overlying mantle^{31,32}, lawsonite is destabilized (700 to 900°C at 8 GPa, Fig. 1a) within the basaltic uppermost layers of the subducting plates. Below, the slower heating of the gabbroic layer enables lawsonite stability for most subduction transects up to ~8 GPa. At higher pressures, the stability of lawsonite little depends on temperature. Thus, in all but the hottest subduction transects (e.g., Cascadia), the oceanic crust crosses its “water line”³³, i.e. the last phase transition beyond which hydrous minerals are unstable, between depths of 250 km and 310 km.

The two petrological models for peridotite display important differences. Below 7 GPa, the formation of the 10-Å phase^{34,35,36} enlarges the temperature range of the stability of hydrous minerals at ~5-6 GPa in the complex model. However, the striking differences impacting H₂O subduction occur in the mineral assemblages above 8 GPa. In the simplified

model, phase A breaks down at approximately 650°C to form brucite, the stability of which increases with pressure. In contrast, in the complex model, brucite is absent. Balangeroite and aluminous phase E form instead²⁴ but within a narrower temperature range compared to that of brucite. These phase assemblages lead to significantly different water lines.

In the thermodynamically (simplified) modeled system, the slope of the water line is negative below 6 GPa and positive above (Fig. 1b). The point of inflection (6 GPa and 580°C), referred to as the “choke point”³⁷, controls the H₂O retention in this system. The Moho-geotherms (Tonga, S. Kurile and Java) passing above or near the choke point are quasi-parallel to the water line at higher P, stabilizing hydrous minerals in the lithospheric mantle within a few kilometers below the Moho. The ability of a subducted-mantle geotherm to pass the choke point has thus been related to its capacity to carry H₂O down to mantle-transition depths, where very high-P hydrous phases (E and D) may be stable over a wide range of temperatures^{5,23,38}.

In the complex peridotite model, the choke point shifts to higher T and P (680°C – 7 GPa, Fig. 1c). This enlarges the range of Moho geotherms stabilizing hydrous minerals up to 6-7 GPa. However, since the phase transition from aluminous-phase E to nominally anhydrous peridotite is quasi-isothermal beyond 8 GPa²⁴, many moderately cold Moho geotherms pass above the choke point but cross the water line between 9 and 12 GPa (e.g. Java). The combined absence of brucite and the quasi-isothermal water line above 8 GPa become thus potential inhibitors to H₂O transport to great depths.

Near-complete dehydration depths

To illustrate the impact of the petrological assumptions, we calculate the depth at which the lowermost-basaltic, the gabbroic and the hydrated peridotitic layers become nearly dry (95% dehydration, see Methods). The latter is assumed to be 4-km thick (~15% serpentinization) in our reference case, following previous studies on GWR³⁹.

The top basaltic layers mainly dry near the depth at which the slab and mantle are kinematically coupled (i.e. at 80–110 km). The dehydration of the gabbros occurs within the depth range of 200-300 km in all but the hottest subduction transects (Fig. 1a). The dehydration pattern of the lithospheric mantle is partly controlled by the thermal state of the transects, but primarily depends on the petrological model. We define three groups of transects based on the way the petrological assumptions impact the mantle-dehydration pattern (Fig. 2).

Most transects belong to group 1, in which the lithospheric mantle dries within the depth range of 120-190 km, assuming the simplified peridotite model. Considering a complex peridotite model, the formation of the 10-Å phase in hot and moderately hot transects (subgroup 1.1) deepens the lithospheric mantle drying by 10 km (Cascadia) to 45 km (NCCChile). Apart from the hottest transects, the H₂O transport is limited by the breakdown of lawsonite in subgroup 1.1. If the 10-Å phase breaks down to balangeroite and aluminous-phase E (moderately cold geotherms, subgroup 1.2), dehydration occurs deeper than in the simplified system and up to 310 km (Ryukyu) when the aluminous-phase E destabilizes. The transects in group 2 (moderately cold to cold geotherms) never dry when assuming a simplified peridotite model, owing to the formation of phase A and brucite. In contrast, the complex peridotite model induces the drying of the lithospheric mantle between 300 and 350-km depths, following the breakdown of the aluminous-phase E. The hydrated mantle in the coldest-slab transects, forming group 3, never dries before reaching the mid-upper mantle regardless of the peridotite model. These coldest transects are the sole able to convey H₂O to the mantle transition zone according to our preferred complex peridotite model.

Global Water Retention

We compare the global H₂O flux predictions to the bounds allowing a relatively stable sea level during the Phanerozoic. The upper limit of $3.6 \pm 0.6 \times 10^8$ Tg/Myr ensures less than 100 m of sea-level decrease⁶ (Extended data Fig.1). The lower limit for GWR is derived from the total degassing of H₂O at mid-ocean ridges and ocean islands ($2.1 \pm 0.8 \times 10^8$ Tg/Myr⁶), which would prevent an increase in sea-level, consistently with the majority of reconstructions of eustatic sea-level for the current eon^{8,9} (although see ref. 10). Hence, we define the admissible GWR range as $2.1\text{--}3.6 \times 10^8$ Tg/Myr.

We first estimate the H₂O fluxes using the complex peridotite model and our reference case assuming a globally uniform 4-km thick hydrated mantle (Fig. 3a). The predicted Global Input of H₂O at the trenches is 12.4×10^8 Tg/Myr, which is consistent with previous estimations considering the additional 10^8 Tg/Myr of H₂O input by sediments⁵.

At a 230-km depth, that is after mantle dehydration in subgroup 1.1, the GWR is 5.7×10^8 Tg/Myr (Fig. 3), driven by both the lithospheric mantle (61%) and by the gabbroic layer (35%). Adding the potential H₂O flux subducted within sediments⁵ (0.3×10^8 Tg/Myr), the resulting GWR at a depth of 230 km clearly overreaches the admissible GWR.

Gabbros (but also basalts and sediments) are all dry by a 300-km depth. Hence, the GWR at a 350-km depth is solely controlled by the lithospheric mantle of the coldest subduction zones (group 3) and equals 1.2×10^8 Tg/Myr (65% of which result from retention in Tonga and South Vanuatu; Extended Data Fig. 2). Our modeled GWR is lesser than the admissible GWR. Note that a slightly modified petrological assumptions (decreasing serpentinization with distance to the Moho and a reduced stability field of hydrous phases near the choke point, Supplementary Information S4.4.3 and S4.4.5) little affect the latter results. Assuming that the GWR was roughly stable through the Phanerozoic^{5,6}, a complex-peridotite model would predict that mantle degassing slightly dominated. For comparison, the GWR computed at a 350-km depth is nearly doubled with the simplified peridotite model (Fig. 4) and thus falls within the range of admissible GWR. As shown below, this observation does not hold anymore when considering a more prominent hydration of the lithospheric mantle, as proposed by multiple observations for natural subduction zones.

Consequences of a high mantle hydration at the subduction trenches on GWR

Extensional earthquakes at the outer rise suggest that hydration mostly occurs within the first 5 km of the oceanic mantle¹⁸. The GWR computed by assuming a globally uniform 6-km thick hydrated mantle lies within the admissible GWR range only when considering the complex peridotite model (Fig. 3b and 4). Our prediction of GWR using a globally-uniform 8-km thick hydrated mantle exceeds this bound (Fig. 4 and see S4.4.1).

We nonetheless acknowledge that a globally uniform thickness of hydrated mantle might be a strong, and perhaps limiting, assumption. A compilation of the available data on the extent of mantle serpentinization at present-day subduction zones (thickness and serpentinization degree), shows indeed a worldwide disparity (Supplementary Information S3.1). We find that the serpentine content of the incoming plate correlates relatively well with a plastic-radius of slab curvature⁴⁰. This result is used to derive a parameterization of the mantle-hydrated thickness for each modeled transect (SI S3.2).

The parameterized thickness of hydrated mantle spans the range 0.8-8.8 km, with a global average of 5.6 km. The corresponding Global Input is similar to that computed with a globally-uniform thickness of 6 km. Because some of the cold subduction zones promoting deep-H₂O retention are also predicted to host a thicker serpentinized mantle (Tonga,

Kermadec), the GWR at a 350-km depth is higher (3.1×10^8 Tg/Myr) than in the uniform case with 6 km (Figure 4). The GWR assuming a more realistic variable-thickness of hydrated mantle nonetheless remains consistent with a modest sea-level decrease. We emphasize that both a worldwide variability in the extent of mantle hydration and the reduced stability field of hydrous phases predicted by the complex petrology around mid-upper mantle PT conditions ensures a modest return of H₂O to the deep-upper mantle via only a few cold subduction zones.

Sensitivity of predicted GWR to warmer conditions of subduction

The mantle temperature near the choke point of the simplified peridotite model ($P \approx 6$ GPa) is crucial for the predictions of deep-H₂O retention, since higher temperatures would lead to the mantle dehydration in the transects of groups 2 and 3. One could then hypothesize that an enhanced dehydration predicted with the simplified peridotite would reduce (or eliminate) the discrepancy between the modeled and the admissible GWR. To test it, we perform additional models with warmer conditions of subduction: a high mantle potential temperature, a shallow coupling depth between the slab and the mantle, and shear heating along the subduction interface (see SI-S5). Deeper than 150 km, this yields an increase in Moho temperatures of 35–70°C at the choke point pressure (6–7 GPa) depending on the transect, if the effective friction coefficient μ is equal to 0.03, and of 45 to 90°C when it is 0.05. Considering a global-uniform serpentinized mantle thickness of 4 km, we find that warmer conditions with $\mu > 0.03$ and a simplified peridotite model leads to a total amount of H₂O retained at a 350-km depth equivalent to the reference thermal conditions and the complex peridotite model (Fig. S14c). However, we note that to reach such an estimate the models need to be tuned to quite extreme warm conditions. We argue that these could hardly be reached in all subduction zones. Moreover, the warmer-condition assumption results in the release of the bound-H₂O in the lithospheric mantle above depths of 200–250 km. It follows that such conditions would imply the quasi-absence of aqueous-fluids available to assist the triggering of intermediate-to-deep seismicity observed beyond 200 km depth in many present-day subduction zones (see SI-S6), which therefore also advocates for the relevance of the complex peridotite model.

The fate of deep-subducted H₂O

We estimate that GWR at mid-upper mantle depths is 10 to 20% of the Global Input and that mantle regassing exceeds mantle degassing only in moderate proportions, including in our preferred model where the local thicknesses of the hydrated mantle in the coldest subduction zones are as high as ~ 9 km. Hence, our novel thermo-petrological models lessen the discrepancies between thermo-petrological modelling of subductions zones, the geophysical evidence of large amounts of H₂O entering the trenches and the geological constraints on a long-term steady sea level.

An underlying assumption of our study is that all the H₂O release above a 350-km depth returns to the surface (i.e. that mantle regassing is entirely controlled by GWR). Other studies assumed instead that part of the released H₂O was conveyed by the downgoing mantle and contributed to mantle regassing⁶. We argue that compaction-driven porous flow may redirect most of the deep-released H₂O towards the arc^{41,42}, whether under the form of aqueous or supercritical fluids⁴³. Some deep-released fluids may nonetheless be conveyed to the mantle transition zone through partitioning into nominally anhydrous minerals (~ 0.1 wt%⁴⁴) but in moderate proportions compared to our estimated GWR.

Finally, our models may help explain other geophysical observations such as the triggering of intermediate-to-deep seismicity. At the global scale, a drop in the number of volume-change-induced earthquakes in oceanic plates beyond mid-upper mantle depths has

been suggested to highlight that only a few dehydration reactions occur in the deep upper mantle^{46,47,48}. Our first-order analysis of global seismicity reveals in fact that the subduction zones of groups 2 and 3 may host a moderate seismic activity within the depth range of 200-350 km, and a weak activity beyond (see SI-S6 – Fig. S15). If the triggering of these earthquakes is favored by dehydrating-slab fluids, we stress that only the dehydration profiles from the complex peridotite model could explain the vertical distribution of seismicity, specially at depths greater than 250 km. Our study also shows that the lithospheric mantle of the coldest slabs (e.g. Tonga, Kermadec or Vanuatu) are the sole H₂O carriers beyond mid-upper mantle depths. This may explain why despite the potential ability of the mantle transition zone to be an important H₂O reservoir^{49,50}, global-seismic surveys only show a heterogeneous hydration of the transition zone⁵¹.

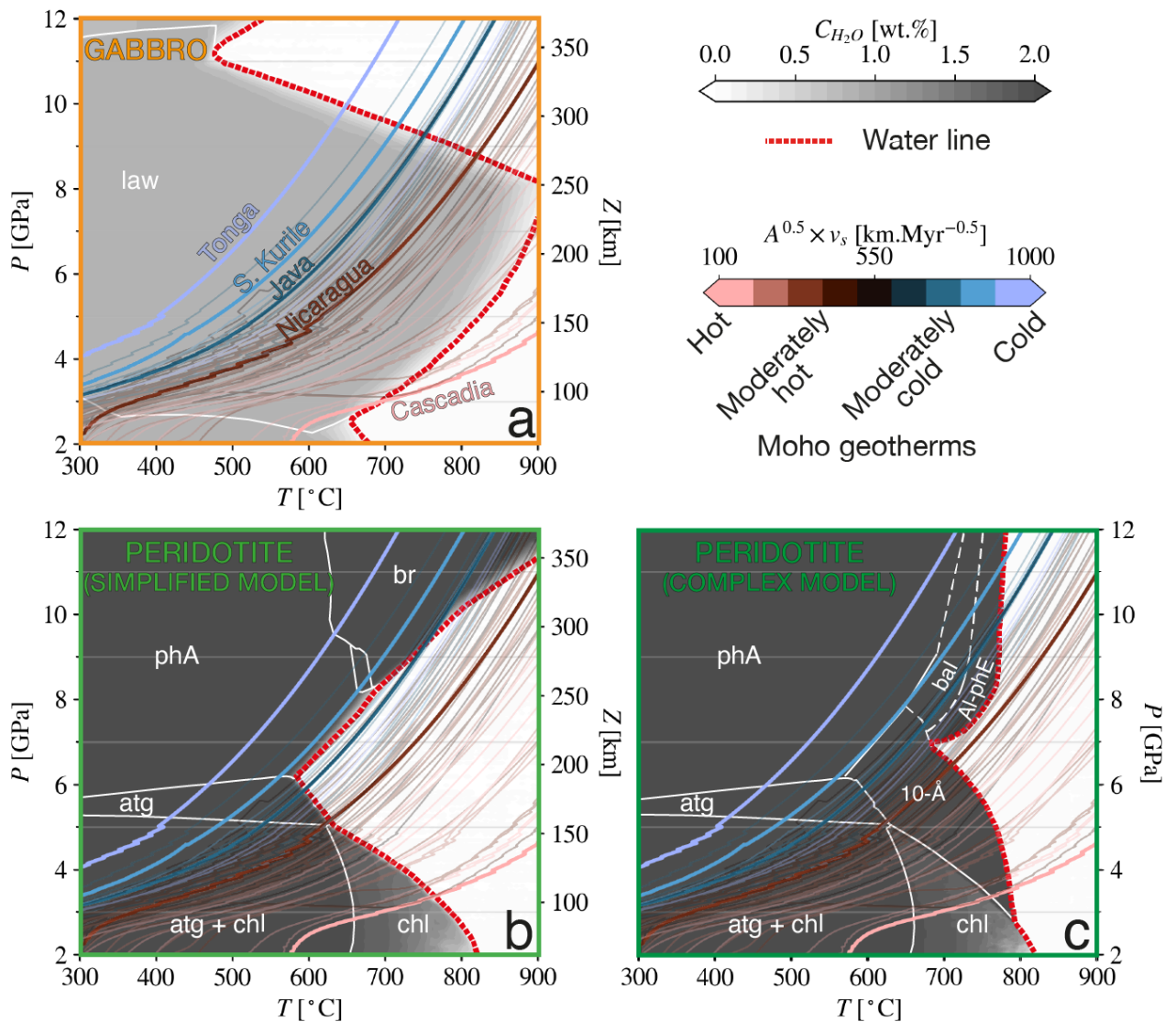


Figure 1 Diagrams of bound-H₂O content for a gabbro (a), a simplified peridotite model (b) and a complex peridotite model (c). The stability fields of the main hydrous phases are depicted by white lines. These are lawsonite (law), antigorite (atg), chlorite (chl), phase A (phA), brucite (br), 10-Å phase (10-Å), balangeroite (bal), and aluminous-phase E (Al-phE). For T lower than 600°C, antigorite and phase A form at pressures lower and higher than 6 GPa, respectively, in both peridotite model^{21,41}. Chlorite is stable at T and P higher than 600°C and lower than 6 GPa. The geotherms at the Moho of the 56 modeled subduction transects are represented by the colored lines, among which five of them have been highlighted using thicker lines. The geotherms are color-coded

following their thermal state, given by the product of the normal convergence rate and the square root of the incoming plate age at trench²⁹.

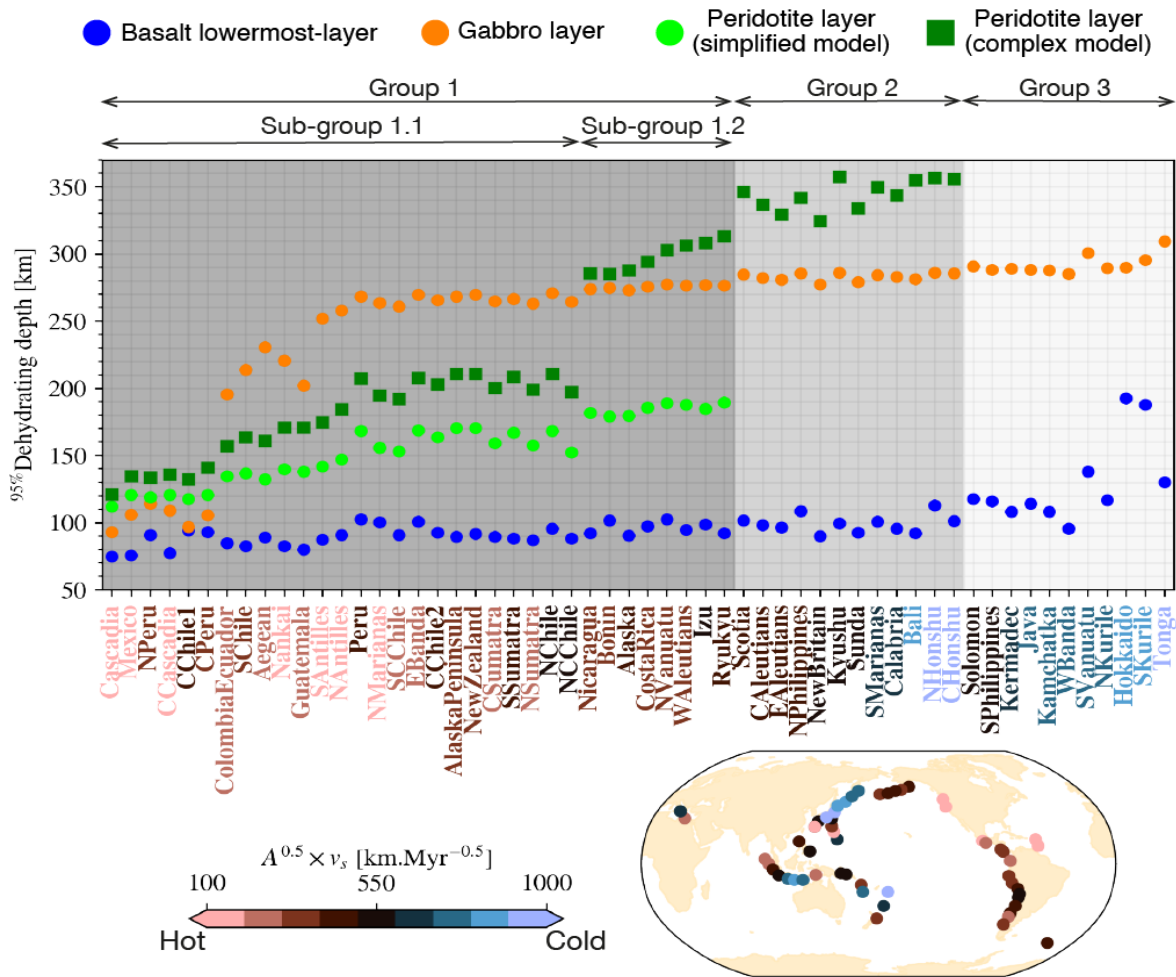


Figure 2: Depth of near-complete (95%) dehydration of the hydrated lithologic layers for each subduction transect. Both the simplified and the complex models are reported for the peridotite. The depth is that of the bottom of the layer when near-complete dehydration occurs. Note that the absence of a symbol means that the layer has not reached a 95% of dehydration. Three groups are defined based on the dehydration mode of the hydrated mantle. Group 1: 95%-dehydration of the mantle regardless peridotite model considered. Group 2: dehydration before 350 km depth only in models with the complex peridotite. Group 3: dehydration of the hydrated mantle does not occur before 350 km depth for any of the models.

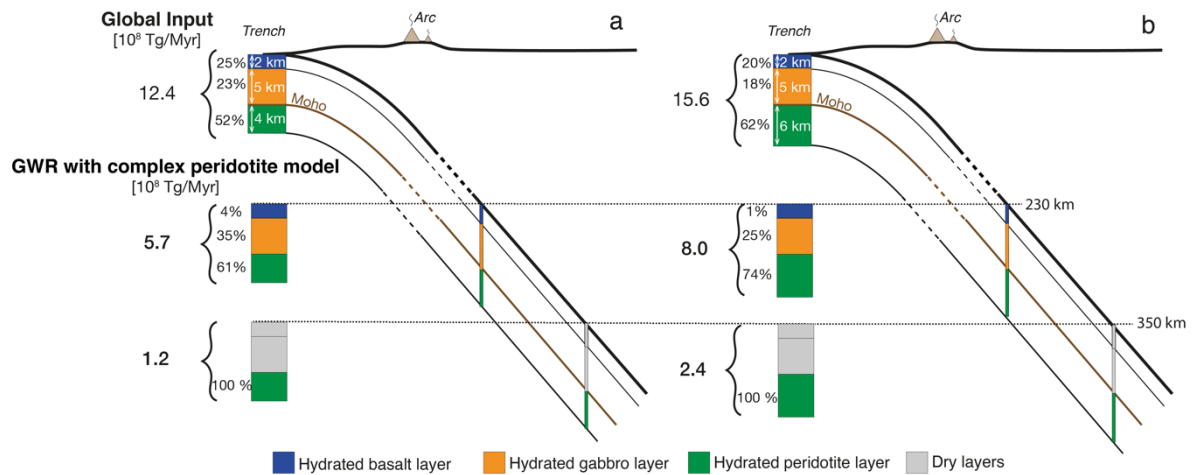


Figure 3: Global input of H_2O at the trenches of present-day subduction zones and global H_2O retention (GWR) computed using a complex peridotite model for the hydrated lithospheric mantle. We display our reference model with a globally uniform thickness of hydrated mantle of 4 km (a) and of 6 km (b).

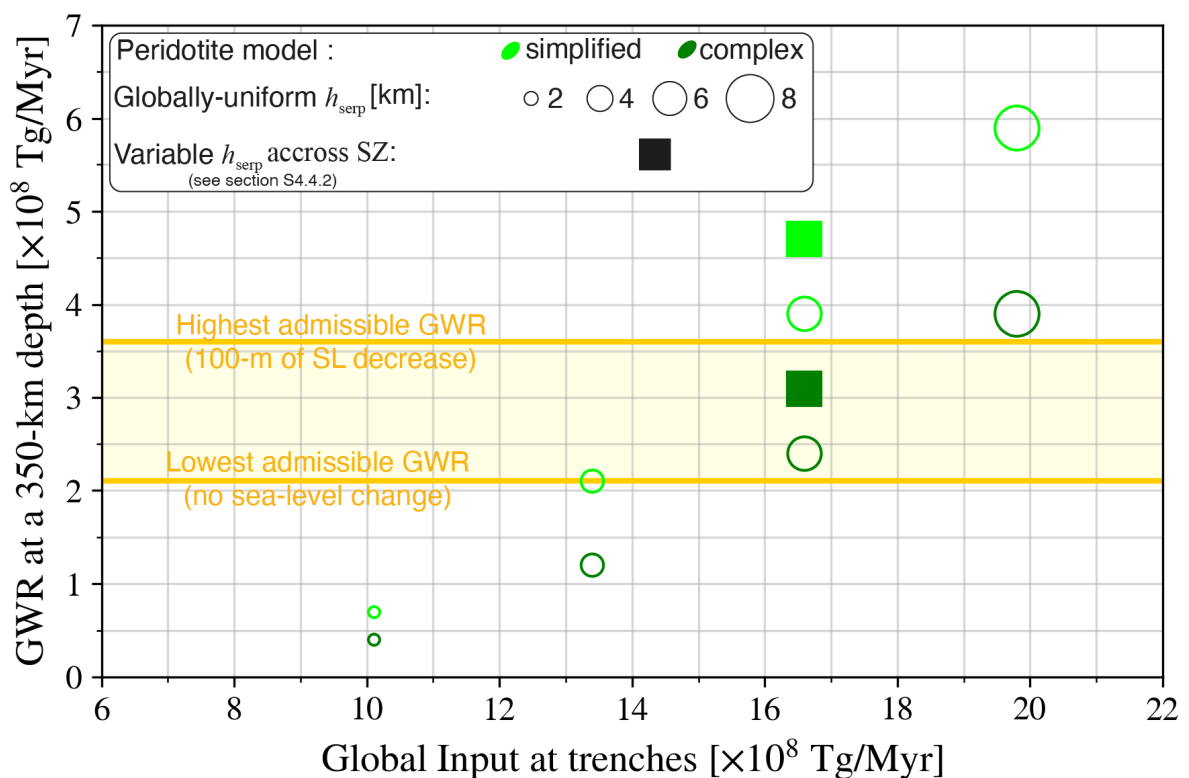


Figure 4: GWR as function of the Global Input at the subduction trenches, depending on the petrological assumptions and the thickness of hydrated mantle at the trenches (see legend).

Methods

Thermal modeling. We consider two-dimensional thermomechanical models in which the kinematics of the subducting slab and of the overriding crust are prescribed while the creeping mantle wedge is dynamic. The mass, momentum and energy conservation equations are solved assuming that mantle flow has reached a steady state⁴² (i.e., solving a steady-state heat equation). We do not include shear heating in the equation of energy, unless specified (see section S5). We consider a composite rheology (diffusion and dislocation) for the wedge where the shear viscosity η is written as

$$\frac{1}{\eta} = \left(\frac{1}{\eta_{diff}} + \frac{1}{\eta_{disl}} + \frac{1}{\eta_{max}} \right)$$

where η_{max} is the maximum viscosity (10^{24} Pa s), and η_{diff} and η_{disl} are the viscosities of diffusion and dislocation creep, respectively. They are given by:

$$\eta_i = \left(A_i b^{-\alpha} C_{OH}^{\beta_i} \exp\left(\frac{E_i}{RT}\right) \right)^{-\frac{1}{\gamma}} \dot{\epsilon}'_{II}^{\left(\frac{1-\gamma}{\gamma}\right)}$$

where the subscript i denotes either diffusion or dislocation creep, b is the grain size, and $\dot{\epsilon}'_{II}$ is the second invariant of the strain rate. A , C_{OH} , E , and R are the preexponential factor, water content, activation energy, and gas constant, respectively. The parameters α , β , and γ are the grain-size, water-content, and stress exponents, respectively. The rheological parameters are set to experimentally determined values for wet olivine (Supplementary Information Table S2).

The discretized problem with finite elements is solved with the software TerraFERMA⁵². We use an unstructured mesh with element sizes ranging from approximately 1 km near the tip of the corner flow to 10 km sufficiently far from the tip where the gradients are smoother.

Thermal-model setup. We perform tests for the 56 transects of major subduction zones defined in previous studies^{5,26}. Our models consist of a fixed rigid upper crust, a subducting slab with a prescribed velocity, and a dynamic viscous mantle wedge that is coupled with the slab below a 75-km depth (Fig. S1), except in the warmer-condition models where we set this depth at 65 km (see section S5). We adopt a realistic geometry for the top of the subducting slab based on the model Slab 2.0⁵³. For consistency, we consider realistic geometries above a 150-km depth. At higher depths, we extrapolate the slab surface with a constant dip to the bottom of the model domain. The imposed subducting slab velocity v_{\square} and upper crust thickness of each modeled transect are as in refs. 5 and 26. The nature (continental vs. oceanic), which defines the boundary condition on the back-arc side as discussed below, and the thickness of the upper plate, as well as the subduction velocity (trench-normal component) and slab age, are taken from ref. 26. The slab thermal structure at the trench is computed following the GDH1 plate cooling model⁵⁴. At the bottom of the slab, we impose the mantle potential temperature $T_m = 1421.5^{\circ}\text{C}$, as in previous estimations of GWR⁵. Note that we also run some models with $T_m = 1450^{\circ}\text{C}$ (see Section S5). The surface temperature is set to 0°C . On the back-arc side, up to the mantle inflow-outflow transition depth, we impose either the GDH1 model when the upper plate is oceanic or a one-dimensional conductive model if the upper plate is continental. The latter temperature boundary condition is capped to the mantle potential temperature. A free-stress boundary condition is imposed on the back-arc side.

Petrological modeling. We adopt a generic lithologic model for the hydrated top of the oceanic plates entering the trench³⁹, which consists of a 2-km thick basaltic layer, a 5-km thick

gabbroic layer, and a globally-uniform thickness (h_{serp}) of the hydrated mantle equals to 4 km in our reference case. We further consider cases with globally-uniform thicknesses of the hydrated mantle equal to 2, 6, and 8 km, as well as a case where h_{serp} varies as a function of the equivalent radius of curvature of the subduction transect (see Supplementary Information S3). The basaltic layer is subdivided into a 0.3-km thick upper volcanic layer, a 0.3-km thick lower volcanic layer, and a 1.4 km thick dike layer, which differ by their initial H₂O contents of 3.1, 2.6, and 1.8 wt. %, respectively. The gabbroic layer has an initial H₂O content of 0.8 wt. %, and the hydrated lithospheric mantle an initial H₂O contents of 2 wt. %, unless otherwise stated. Note that a H₂O content in the lithospheric mantle of 2 wt. % corresponds to approximately 18% serpentinization, which is consistent with serpentinization degrees inferred from geophysical observations³⁹. The phase relations are computed with the thermodynamic code *Perple_X*²⁸ using the thermodynamic database of ref 27. More details on the thermodynamic calculations are given in Supplementary Information. For the complex peridotite model, we combine the phase assemblages predicted by thermodynamic calculations to experimental data on phase relations at high PT obtained from natural serpentinites containing magnetite²⁴ (see below).

Complex (natural) peridotite modeling. We first compile available experimental data on phase assemblages in natural²⁴ and modeled peridotite systems containing Fe³⁺, Al, Ca and Na^{35,36} at temperatures higher than 600 °C and pressures higher than 4 GPa (see Fig. S2b). These reported phase relations serve as a basis for modifying the pseudosections modeled using *Perple_X* under these conditions (Fig. S2a). Given the lack of experimental data in the range of 6.5 to 8 GPa, we derive two approximate phase transitions (10-Å phase to olivine and Al-bearing phase E to olivine) by implementing at these P-T conditions: a high (HMmax) and a conservative (HMmin) estimate of the extent of the stability field of the hydrous phases (Fig. S2c). Note that our calculations of GWR in the main text are mostly based on the high-estimate case HMmax, but we also performed calculations with the low estimate. Mass balances are performed to infer the H₂O contents in the modified phase assemblages (Fig. S2c).

Calculation of the H₂O fluxes. We adopt the approach of ref. 55 to calculate the H₂O distribution in the two-dimensional subduction models. The hydrated portion of the subducting slab is divided into 500-m wide vertical columns. The columns are further subdivided into cells with a height of 100 m. We then calculate the mass of H₂O retained by each cell given the PT conditions at its center. The total mass of the H₂O retained in each column (or a lithologic layer) is given by a summation of the H₂O content of the cells and converted into a mass flux (in Tg/Myr/m) by using the horizontal projection of the subduction velocity at the top of the column. Note that, in our approach, the H₂O mass flux (H₂O/water retention) at a given depth is that of the vertical column for which the top lies at this depth. We do not consider the rehydration of previously dehydrated cells⁵⁰. We choose to compute the 95% dehydration depth instead of full dehydration to analyze the dehydration pattern of the hydrated lithologic layers (Fig. 2) for two reasons. First, in the mafic lithologies, phengite is stable up to 9.5 GPa and can retain residual amounts of H₂O (<0.2 wt.%) after lawsonite breaks down. Thus, the depth of total dehydration would not illustrate the condition at which most of the H₂O is released from the mafic lithologies. Second, our calculation of the H₂O content may also suffer from minor numerical artifacts which may lead to artificial residual amounts of H₂O retained in the computing cells, although the PT conditions of dehydration are reached. Finally, to calculate the GWR, we multiply the retention modeled for each transect by the corresponding length given by ref 26. Note that the 4 wt.% of GWR within the

basaltic crust at a 230-km depth is due to both small amounts of actual H₂O retention by phengite and minor numerical artifacts.

References

- 1 Hirth, G., & Kohlstedt, D. (2003). Rheology of the upper mantle and the mantle wedge: A view from the experimentalists. *Geophysical Monograph-American Geophysical Union*, **138**, 83-106. <https://doi.org/10.1029/138GM06>
- 2 Regenauer-Lieb, K., Yuen, D. A., & Branlund, J. (2001). The initiation of subduction: criticality by addition of water?. *Science*, **294(5542)**, 578-580. <https://doi.org/10.1126/science.1063891>
- 3 Kasting, J. F., & Catling, D. (2003). Evolution of a habitable planet. *Annual Review of Astronomy and Astrophysics*, **41(1)**, 429-463. <https://doi.org/10.1146/annurev.astro.41.071601.170049>
- 4 Conrad, C. P. (2013). The solid Earth's influence on sea level. *Bulletin*, **125(7-8)**, 1027-1052. <https://doi.org/10.1130/B30764.1>
- 5 van Keken, P. E., Hacker, B. R., Syracuse, E. M., & Abers, G. A. (2011). Subduction factory: 4. Depth-dependent flux of H₂O from subducting slabs worldwide. *J. of Geophys. Res.: Solid Earth*, **116(B1)**. <https://doi.org/10.1029/2010JB007922>
- 6 Parai, R. I. T. A., & Mukhopadhyay, S. U. J. O. Y. (2012). How large is the subducted water flux? New constraints on mantle regassing rates. *Earth and Planet. Sc. Lett.*, **317**, 396-406. <https://doi.org/10.1016/j.epsl.2011.11.024>
- 7 Hirschmann, M. M. (2018). Comparative deep Earth volatile cycles: The case for C recycling from exosphere/mantle fractionation of major (H₂O, C, N) volatiles and from H₂O/Ce, CO₂/Ba, and CO₂/Nb exosphere ratios. *Earth and Planet. Sc. Lett.*, **502**, 262-273. <https://doi.org/10.1016/j.epsl.2018.08.023>
- 8 Vail, P. R., Mitchum Jr, R. M., & Thompson III, S. (1977). Seismic stratigraphy and global changes of sea level: Part 4. Global cycles of relative changes of sea level.: Section 2. Application of seismic reflection configuration to stratigraphic interpretation.
- 9 Hallam, A. (1992). Phanerozoic sea-level changes. Columbia University Press.
- 10 Haq, B. U., & Schutter, S. R. (2008). A chronology of Paleozoic sea-level changes. *Science*, **322(5898)**, 64-68. <https://doi.org/10.1126/science.1161648>
- 11 Karlsen, K. S., Conrad, C. P., & Magni, V. (2019). Deep water cycling and sea level change since the breakup of Pangea. *Geochem., Geophys., Geosyst.*, **20(6)**, 2919-2935. <https://doi.org/10.1029/2019GC008232>
- 12 Rüpke, L. H., Morgan, J. P., Hort, M., & Connolly, J. A. (2004). Serpentine and the subduction zone water cycle. *Earth and Planet. Sc. Lett.*, **223(1-2)**, 17-34. <https://doi.org/10.1016/j.epsl.2004.04.018>
- 13 Faccenda, M., Gerya, T. V., & Burlini, L. (2009). Deep slab hydration induced by bending-related variations in tectonic pressure. *Nature Geoscience*, **2(11)**, 790-793. <https://doi.org/10.1038/ngeo656>
- 14 Magni, V., Bouilhol, P., & van Hunen, J. (2014). Deep water recycling through time. *Geochem., Geophys., Geosyst.*, **15(11)**, 4203-4216. <https://doi.org/10.1002/2014GC005525>
- 15 Wallace, P. J. (2005). Volatiles in subduction zone magmas: concentrations and fluxes based on melt inclusion and volcanic gas data. *J. of volcanology and Geothermal Res.*, **140(1-3)**, 217-240. <https://doi.org/10.1016/j.jvolgeores.2004.07.023>

- 16 Ranero, C. R., Morgan, J. P., McIntosh, K., & Reichert, C. (2003). Bending-related faulting and mantle serpentinization at the Middle America trench. *Nature*, **425(6956)**, 367-373. <https://doi.org/10.1038/nature01961>
- 17 Contreras-Reyes, E., Grevemeyer, I., Flueh, E. R., & Reichert, C. (2008). Upper lithospheric structure of the subduction zone offshore of southern Arauco peninsula, Chile, at ~38°S. *J. of Geophys. Res.: Solid Earth*, **113(B7)**. <https://doi.org/10.1029/2007JB005569>
- 18 Emry, E. L., & Wiens, D. A. (2015). Incoming plate faulting in the Northern and Western Pacific and implications for subduction zone water budgets. *Earth and Planet. Sc. Lett.*, **414**, 176-186. <https://doi.org/10.1016/j.epsl.2014.12.042>
- 19 Cai, C., Wiens, D. A., Shen, W., & Eimer, M. (2018). Water input into the Mariana subduction zone estimated from ocean-bottom seismic data. *Nature*, **563(7731)**, 389-392. <https://doi.org/10.1038/s41586-018-0655-4>
- 20 Hermann, J., & Lakey, S. (2021). Water transfer to the deep mantle through hydrous, Al-rich silicates in subduction zones. *Geology*. <https://doi.org/10.1130/G48658.1>
- 21 Schmidt, M. W., & Poli, S. (1998). Experimentally based water budgets for dehydrating slabs and consequences for arc magma generation. *Earth and Planet. Sc. Lett.*, **163(1-4)**, 361-379. [https://doi.org/10.1016/S0012-821X\(98\)00142-3](https://doi.org/10.1016/S0012-821X(98)00142-3)
- 22 Okamoto, K., & Maruyama, S. (1999). The high-pressure synthesis of lawsonite in the MORB+ H₂O system. *American Mineralogist*, **84(3)**, 362-373. <https://doi.org/10.2138/am-1999-0320>
- 23 Iwamori, H. (2004). Phase relations of peridotites under H₂O-saturated conditions and ability of subducting plates for transportation of H₂O. *Earth and Planet. Sc. Lett.*, **227(1-2)**, 57-71. <https://doi.org/10.1016/j.epsl.2004.08.013>
- 24 Maurice, J., et al. (2018). The stability of hydrous phases beyond antigorite breakdown for a magnetite-bearing natural serpentinite between 6.5 and 11 GPa. *Contributions to Mineralogy and Petrology*, **173(10)**, 86. <https://doi.org/10.1007/s00410-018-1507-9>
- 25 Maurice, J., et al. (2020). The intrinsic nature of antigorite breakdown at 3 GPa: Experimental constraints on redox conditions of serpentinite dehydration in subduction zones. *Contributions to Mineralogy and Petrology*, **175(10)**, 1-23. <https://doi.org/10.1007/s00410-020-01731-y>
- 26 Syracuse, E. M., van Keken, P. E., & Abers, G. A. (2010). The global range of subduction zone thermal models. *Phys. Earth Planet. Inter.*, **183(1-2)**, 73-90. <https://doi.org/10.1016/j.pepi.2010.02.004>
- 27 Holland, T. J. B., & Powell, R. (2011). An improved and extended internally consistent thermodynamic dataset for phases of petrological interest, involving a new equation of state for solids. *J. of Metamorphic Geology*, **29(3)**, 333-383. <https://doi.org/10.1111/j.1525-1314.2010.00923.x>
- 28 Connolly, J. A. D. (2009). The geodynamic equation of state: what and how. *Geochem., Geophys., Geosyst.*, **10(10)**. <https://doi.org/10.1029/2009GC002540>
- 29 Maunder, B., van Hunen, J., Bouilhol, P., & Magni, V. (2019). Modeling slab temperature: A reevaluation of the thermal parameter. *Geochem., Geophys., Geosyst.*, **20(2)**, 673-687. <https://doi.org/10.1029/2018GC007641>
- 30 Schmidt, M., & Poli, S. (2013). Devolatilization during subduction. <https://doi.org/10.1016/B978-0-08-095975-7.00321-1>

- 31** Wada, I., & Wang, K. (2009). Common depth of slab-mantle decoupling: Reconciling diversity and uniformity of subduction zones. *Geochem., Geophys., Geosyst.*, **10(10)**. <https://doi.org/10.1029/2009GC002570>
- 32** Arcay, D. (2012). Dynamics of interplate domain in subduction zones: influence of rheological parameters and subducting plate age. *Solid Earth*, **3(2)**, 467-488. <https://doi.org/10.1016/j.epsl.2006.12.027>
- 33** Liu, L. G. (1987). Effects of H₂O on the phase behaviour of the forsterite-enstatite system at high pressures and temperatures and implications for the Earth. *Phys. Earth Planet. Inter.*, **49(1-2)**, 142-167. [https://doi.org/10.1016/0031-9201\(87\)90138-5](https://doi.org/10.1016/0031-9201(87)90138-5)
- 34** Ulmer, P., & Trommsdorff, V. (1995). Serpentine stability to mantle depths and subduction-related magmatism. *Science*, 268(5212), 858-861. <https://doi.org/10.1126/science.268.5212.858>
- 35** Fumagalli, P., & Poli, S. (2005). Experimentally determined phase relations in hydrous peridotites to 6·5 GPa and their consequences on the dynamics of subduction zones. *J. of Petrology*, **46(3)**, 555-578. <https://doi.org/10.1093/petrology/egh088>
- 36** Dvir, O., Pettke, T., Fumagalli, P., & Kessel, R. (2011). Fluids in the peridotite–water system up to 6 GPa and 800 C: new experimental constrains on dehydration reactions. *Contrib. to Mineralogy and Petrology*, **161(6)**, 829-844. <https://doi.org/10.1007/s00410-010-0567-2>
- 37** Kawamoto, T., Hervig, R. L., & Holloway, J. R. (1996). Experimental evidence for a hydrous transition zone in the early Earth's mantle. *Earth and Planet. Sc. Lett.*, **142(3-4)**, 587-592. [https://doi.org/10.1016/0012-821X\(96\)00113-6](https://doi.org/10.1016/0012-821X(96)00113-6)
- 38** Komabayashi, T., & Omori, S. (2006). Internally consistent thermodynamic data set for dense hydrous magnesium silicates up to 35 GPa, 1600 C: implications for water circulation in the Earth's deep mantle. *Phys. Earth Planet. Inter.*, **156(1-2)**, 89-107. <https://doi.org/10.1016/j.pepi.2006.02.002>
- 39** Hacker, B. R. (2008). H₂O subduction beyond arcs. *Geochem., Geophys., Geosyst.*, **9(3)**. <https://doi.org/10.1029/2007GC001707>
- 40** Buffett, B. A., & Heuret, A. (2011). Curvature of subducted lithosphere from earthquake locations in the Wadati-Benioff zone. *Geochemistry, Geophysics, Geosystems*, **12(6)**. <https://doi.org/10.1029/2011GC003570>
- 41** Wilson, C. R., Spiegelman, M., van Keken, P. E., & Hacker, B. R. (2014). Fluid flow in subduction zones: The role of solid rheology and compaction pressure. *Earth and Planet. Sc. Lett.*, **401**, 261-274. <https://doi.org/10.1016/j.epsl.2014.05.052>
- 42** Cerpa, N. G., Wada, I., & Wilson, C. R. (2017). Fluid migration in the mantle wedge: Influence of mineral grain size and mantle compaction. *J. of Geophys. Res.: Solid Earth*, **122(8)**, 6247-6268. <https://doi.org/10.1002/2017JB014046>
- 43** Mibe, K., Kanzaki, M., Kawamoto, T., Matsukage, K. N., Fei, Y., & Ono, S. (2007). Second critical endpoint in the peridotite-H₂O system. *Journal of Geophysical Research: Solid Earth*, **112(B3)**. <https://doi.org/10.1029/2005JB004125>
- 44** Padrón-Navarta, J. A., & Hermann, J. (2017). A subsolidus olivine water solubility equation for the Earth's upper mantle. *J. of Geophys. Res.: Solid Earth*, **122(12)**, 9862-9880. <https://doi.org/10.1002/2017JB014510>
- 46** Omori, S., Komabayashi, T., & Maruyama, S. (2004). Dehydration and earthquakes in the subducting slab: empirical link in intermediate and deep seismic zones. *Phys. Earth Planet. Inter.*, **146(1-2)**, 297-311. <https://doi.org/10.1016/j.pepi.2003.08.014>

- 47 Green II, H. W., Chen, W. P., & Brudzinski, M. R. (2010). Seismic evidence of negligible water carried below 400-km depth in subducting lithosphere. *Nature*, **467(7317)**, 828-831. <https://doi.org/10.1038/nature09401>
- 48 Ferrand, T. P. (2019). Seismicity and mineral destabilizations in the subducting mantle up to 6 GPa, 200 km depth. *Lithos*, 334, 205-230. <https://doi.org/10.1016/j.lithos.2019.03.014>
- 49 Smyth, J. R., Holl, C. M., Frost, D. J., Jacobsen, S. D., Langenhorst, F., & Mccammon, C. A. (2003). Structural systematics of hydrous ringwoodite and water in Earth's interior. *American Mineralogist*, **88(10)**, 1402-1407. <https://doi.org/10.2138/am-2003-1001>
- 50 Fei, H., & Katsura, T. (2020). High water solubility of ringwoodite at mantle transition zone temperature. *Earth and Planetary Science Letters*, **531**, 115987. <https://doi.org/10.1016/j.epsl.2019.115987>
- 51 Houser, C. (2016). Global seismic data reveal little water in the mantle transition zone. *Earth and Planet. Sc. Lett.*, **448**, 94-101. <https://doi.org/10.1016/j.epsl.2016.04.018>

Methods references

- 52 Wilson, C. R., Spiegelman, M., & van Keken, P. E. (2017). Terra FERMA: The Transparent Finite Element Rapid Model Assembler for multiphysics problems in Earth sciences. *Geochem., Geophys., Geosyst.*, **18(2)**, 769-810. doi :10.1002/2016GC006702
- 53 Hayes, G. P., et al. (2018). Slab2, a comprehensive subduction zone geometry model. *Science*, **362(6410)**, 58-61. doi: 10.1126/science.aat4723
- 54 Stein, C. A., & Stein, S. (1992). A model for the global variation in oceanic depth and heat flow with lithospheric age. *Nature*, **359(6391)**, 123-129. doi:10.1038/359123a0
- 55 Wada, I., Behn, M. D., & Shaw, A. M. (2012). Effects of heterogeneous hydration in the incoming plate, slab rehydration, and mantle wedge hydration on slab-derived H₂O flux in subduction zones. *Earth and Planet. Sc. Lett.*, **353**, 60-71. doi :10.1016/j.epsl.2012.07.025
- 56 Cramer, F. (2018). Scientific colour-maps. *Zenodo*. <http://doi.org/10.5281/zenodo.1243862>

Code availability. The code TerraFERMA used to compute the thermal models is open-source and available here <http://terraferma.github.io/>. The thermodynamic code Perple_X is freely available here <http://www.perplex.ethz.ch/> and information to reproduce the results are provided in the Methods section and in the Supplementary Information.

Data availability. The numerical data generated for the 56 subduction transects (geotherms and water retention within the subducting slabs) will be made available at a public repository upon acceptance of publication.

Acknowledgments. The authors would like to thank Andrea Tommasi and Serge Lallemand for their very useful suggestions, and Stéphane Arnal and Fabien Rétif for their assistance in installing the code on the clusters. This study was publicly funded by through ANR under the “Investissements d’avenir,

Initiative Sciences Innovation Territoires—MUSE” program with the reference ANR-16-IDEX-0006. The work has been realized with the support of the HPC Platform MESO@LR, financed by the Occitanie / Pyrénées-Méditerranée Region, Montpellier Mediterranean Metropole and the University of Montpellier. Perceptually uniform color maps were used in some figures of this study to prevent visual distortion of the data⁵¹.

Author contributions. N. C. conceived the study, designed and performed the numerical models, analyzed the results, and wrote the first draft of the paper. D. A. provided funding for the project, participated to conceive the study and analyzed the results. J. A. P.-N. contributed to the petrological modeling and to the analysis of the results. All authors discussed the implications of the study and participated to the writing of the paper.

Extended Data Fig. 0: The first row displays the average change in sea level over the Phanerozoic derived from geological constraints. The second and third row provide bounds on the GWR (admissible GWR) compatible with a 0 to 100-m of change in sea-level. Note that the asterisk (2nd row) denotes an indirect bound where we have assumed that a 0-m change of sea level over the Phanerozoic will be achieved if the GWR is equal to the total H₂O degassing both at mid-ocean ridges and at ocean islands. The fourth row shows the estimated GWR by the thermo-petrological models of ref. 5.

Study	Mean sea level change over the last 542 Ma	Global Input [10 ⁸ Tg/Myr]	GWR [10 ⁸ Tg/Myr]
refs. 8,9,10	-75 m (average from ref. 6)		
ref. 7	0 m*		2.1*
ref. 6	0 m -100 m	10.8	2.5 3.6
ref. 5		10.0	3.4

Extended data Fig. 2: H_2O retention per subduction zone at depths of 230 km (a) and 350 km (b) assuming a globally-uniform thickness of 4 km for the hydrated mantle. The calculations with our two peridotite models are displayed. The names of the subduction zones are color-coded as a function of their thermal state (see Fig. 1).

